Linear magnetoresistance induced by mobility fluctuations in iodine-intercalated tungsten ditelluride

W. L. Zhu,[1,*] Y. Cao,[1] P. J. Guo,[2] X. Li,[1] Y. J. Chen,[3] L. J. Zhu,[1] J. B. He,[4] Y. F. Huang,[5,6] Q. X. Dong,[5,6] Y. Y. Wang,[7] R. Q. Zhai,[1] Y. B. Ou,[1] G. Q. Zhu,[1] H. Y. Lu,[3] G. Li,[2,5,6] G. F. Chen,[2,5,6,†] and M. H. Pan[1,‡]

[1]*School of Physics and Information Technology, Shaanxi Normal University, Xi'an 710062, China*
[2]*Songshan Lake Materials Laboratory, Dongguan, Guangdong 523808, China*
[3]*School of Physics and Physical Engineering, Qufu Normal University, Qufu 273165, China*
[4]*College of Physics and Electronic Engineering, Nanyang Normal University, Nanyang 473061, China*
[5]*Institute of Physics and Beijing National Laboratory for Condensed Matter Physics, Chinese Academy of Sciences, Beijing 100190, China*
[6]*School of Physical Sciences, University of Chinese Academy of Sciences, Beijing 100049, China*
[7]*Institute of Physical Science and Information Technology, Anhui University, Hefei, Anhui 230601, China*

(Received 16 December 2021; accepted 2 March 2022; published 14 March 2022)

We report a systematic study of the magnetoresistance, Hall effect, and the electronic structure in an iodine-intercalated tungsten ditelluride (WTe_2I) single crystal, which crystallizes in a centrosymmetric structure. WTe_2I presents significant anisotropic magnetotransport behavior with the magnetic field rotated in the xz and yz planes and violation of the Kohler's rule. Unexpectedly, nonsaturating linear magnetoresistance (LMR) was observed under the magnetic field parallel to the z axis and the current along the x axis. The analysis of the Hall effect reveals that the carrier mobility in WTe_2I is notably lower than that of WTe_2 and meets the picture of the Parrish and Littlewood model, suggesting that the LMR is likely caused by disorder effects. First-principles calculations show that the electronic structure undergoes a topological phase transition from a Weyl state to a Dirac state due to iodine intercalation. This finding provides a platform to search for physical phenomena related to WTe_2 and study the topological phase transition.

DOI: 10.1103/PhysRevB.105.125116

I. INTRODUCTION

Materials with a nontrivial band structure sparked intense research interests in condensed matter physics and material science due to exotic physical properties and potential applications [1–5]. Their topologically protected band structures are featured with a degeneracy and momentum space distribution of the nodal points, which not only themselves present fascinating electronic states, but also provide the possibility to realize some novel quantum states by various methods, such as doping, gating, point contact, and high pressure [6–8]. Among the emergent phenomena, linear magnetoresistance (LMR) is of particular interest. LMR, an unusual behavior beyond classical quadratic magnetoresistance (QMR), has also been observed in limited narrow gap semiconductors and several common metals such as silver chalcogenides [9–11], Sb-rich InSb [12], polycrystalline potassium [13], and $BaZnBi_2$ [14], and in these materials has usually been interpreted by either the charge-inhomogeneity theory [15] or Abrikosov's quantum theory [16]. However, LMR in topological materials (TMs) can be more intriguing due to the involvement of nontrivial electronic states, as an external magnetic field could lift the protection against backscattering, while the Landau level diagram with the magnetic field aligned in a high-symmetry direction could be gapless [17]. The pindown of the LMR mechanism is further hindered since there exist nontrivial electronic states and disorder-induced or carrier-compensation-induced magnetoresistance (MR) [17–24]. Thus, a further exploration of a TM with a tunable electronic structure while hosting LMR is of interest.

The semimetal WTe_2, a typical TM, has been studied intensively due to the discovery of the unexpected property of large unsaturated transverse QMR and longitudinal LMR [24,25]. WTe_2 crystallizes in a layered structure with the metal layer sandwiched by adjacent chalcogenide layers. The coupling between the Te-W-Te sandwich layer is weak van der Waals bonding, which allows for the realization of atom or ion intercalation for carrier doping and cleavage for device fabrication. On the other hand, the band structure in WTe_2 characterized by small electron and hole pockets is very sensitive to the position of the Fermi level and is easy to modulate in some ways. These unique crystal and band structures result in many interesting properties including gate- and pressure-induced superconductivity [26,27], Landau quantization and highly mobile fermions in a monolayer WTe_2 [28], gate-tunable negative longitudinal MR [29], and vacancy- and pressure-induced transverse LMR [30,31]. Such findings suggest that a different way to study the LMR in TMs is by tuning the electronic structure based on WTe_2.

The intercalation of van der Waals materials may allow one to effectively adjust the electronic structure and physical properties. Recently, Schmidt synthesized iodine-intercalated

*wlzhu@snnu.edu.cn
†gfchen@iphy.ac.cn
‡minghupan@snnu.edu.cn

tungsten ditelluride (WTe_2I) and found that its band structures have some differences from that of WTe_2 [32], which are highly significant to further understand the MR behavior in WTe_2. However, magnetotransport studies on WTe_2I are still absent. In this paper, we have grown single crystals of WTe_2I and systematically investigated its magnetotransport properties with temperatures ranging from 2 to 300 K at magnetic fields up to 9 T. We observed anisotropic magnetotransport behavior in different magnetic field directions. Remarkably, when the applied magnetic fields are along the z axis, the positive $\mathrm{MR}(B) = [\rho_{xx}(B) - \rho_{xx}(0)]/\rho_{xx}(0) \times 100\%$ exhibits an unsaturated linear behavior at 2 K. The analysis of Hall resistivity and longitudinal conductivity with a semiclassical two-band model indicates that iodine intercalation leads to a decrease of the carrier mobility. The values of the observed LMR, mobility, and the reciprocal of the crossover field show a similar temperature-dependent tendency. This suggests that the unsaturated LMR in WTe_2I probably originates from mobility fluctuations caused by the disorder. In addition, the electronic structure of WTe_2I has been studied by first-principles calculations. The band structure shows that WTe_2I is a metal and the band at the high-symmetry Z point is a fourfold-degenerate Dirac point.

II. EXPERIMENTAL METHODS AND CRYSTAL STRUCTURE

Single crystals of WTe_2I were obtained by intercalating iodine into WTe_2 crystals, which were grown from Te flux. A 1:30 mixture of W and Te was put into an alumina crucible and sealed in an evacuated quartz tube. The quartz tube was heated to 850 °C and then cooled at a speed of 1 °C/h to 550 °C, at which point the excess Te was decanted by centrifugation. Subsequently, the obtained WTe_2 single crystals were filled in a quartz tube with an iodine concentration of 3 mg/cm^3. After evacuating and sealing, the tube was heated to 120 °C for 20 days, and then cooled down to room temperature. The resulting crystals of WTe_2I are thin strips with a length ~1.6 mm and thickness ~0.12 mm, as shown in the right inset of Fig. 1(c). The crystal structure was characterized by x-ray diffraction (XRD) on a Bruker diffractometer with Cu $K\alpha$ radiation at room temperature. The elemental composition was determined by an Oxford X-Max energy dispersive x-ray (EDX) spectroscopy analysis on a Hitachi S-4800 scanning electron microscope. Electrical transport measurements on oriented single crystals were performed using a Quantum Design physical property measurement system (PPMS).

First-principles calculations were performed with the projector augmented-wave method [33,34] as implemented in the Vienna *ab initio* simulation package [35–37]. The generalized gradient approximation of Perdew-Burke-Ernzerhof type [38] was adopted for the exchange-correlation potential. The optB86b functional [39] was used to treat the van der Waals interactions in layered materials. The kinetic energy cutoff of the plane-wave basis was set to be 400 eV. For the Brillouin zone sampling, a $20 \times 12 \times 4$ k-point mesh was employed. The Gaussian smearing with a width of 0.01 eV was used around the Fermi surface. In the structural optimization, both cell parameters and internal atomic positions were allowed

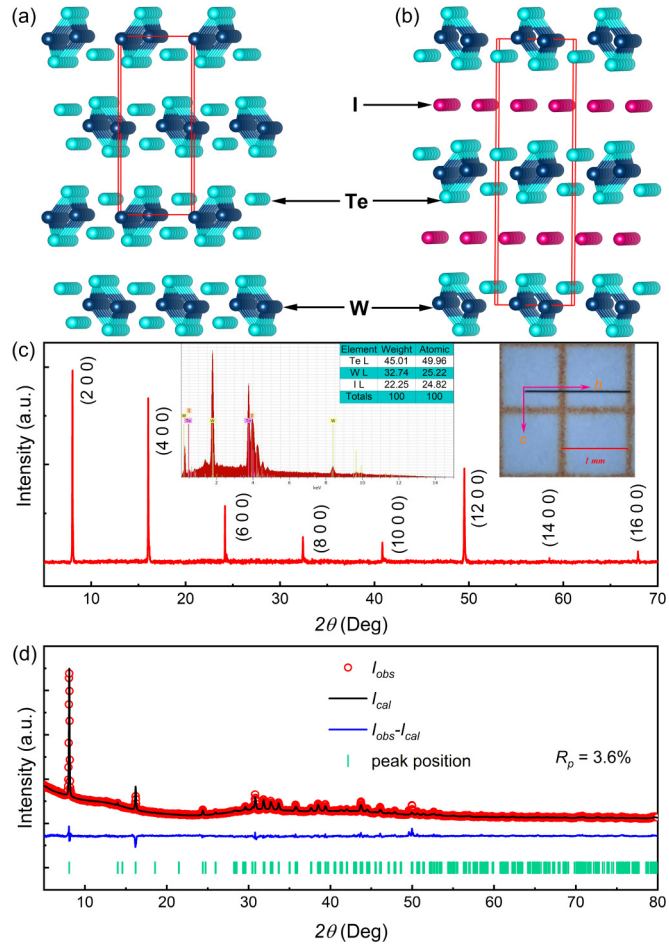

FIG. 1. (a) and (b) The crystal structure of WTe_2 and WTe_2I at room temperature, respectively. (c) The single-crystal XRD pattern of WTe_2I at room temperature. The left inset is the EDX spectroscopy of WTe_2I. The right inset is an optical image of a grown single crystal with respect to the crystalline axes on a millimeter grid. (d) Powder XRD spectrum of WTe_2I at room temperature and refinement.

to relax until all forces on the atoms were smaller than 0.01 eV/Å. The relaxed structure parameters a, b, and c are 21.587, 3.475, and 6.270 Å, respectively, which well agree with experimental results. The spin-orbital-coupling effect was included in the calculations of the electronic properties.

Figure 1(b) shows the crystal structure of WTe_2I crystallizing in a layer orthorhombic structure with a centrosymmetric space group *Pmmn* (No. 59). The layer structure is closely similar to that of WTe_2 [Fig. 1(a)] but contains iodine atoms in interlayers. The single-crystal XRD pattern of a WTe_2I sample is presented in Fig. 1(c). All of the peaks can be identified as the (h00) reflections of WTe_2I. Figure 1(d) shows the room-temperature powder XRD pattern of the ground WTe_2I single crystals, in which all the powder diffraction peaks can be well indexed in a *Pmmn* space group. The determined lattice parameters $a = 21.897$ Å, $b = 3.476$ Å, and $c = 6.327$ Å are in good agreement with the previously reported data [32]. The average W:Te:I atomic ratio determined using the EDX is very close to 1:2:1 and no foreign elements were detected

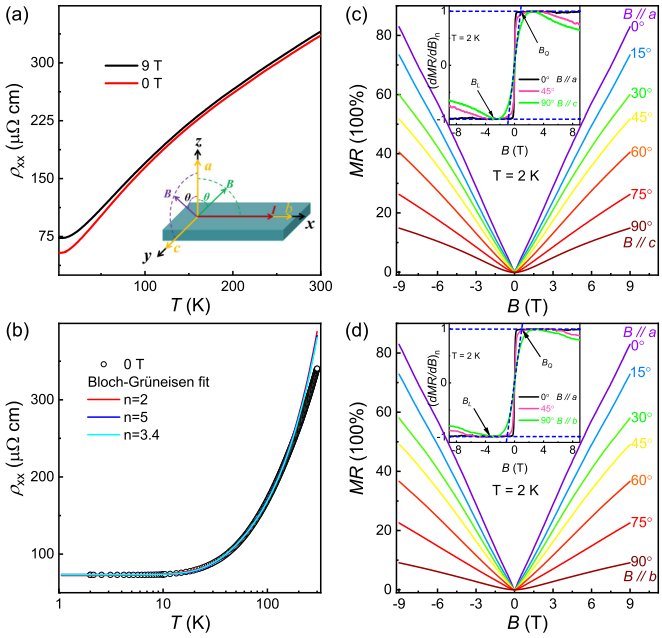

FIG. 2. (a) Temperature dependence of ρ_{xx} under magnetic fields with $B \parallel z$ axis. The inset illustrates measurement configuration. (b) Bloch-Grüneisen fit of zero field $\rho(T)$ (see text). (c) and (d) Magnetic field dependence of MR at 2 K with B rotated in the yz and xz planes, respectively. Insets show the B dependence of the normalized derivative of MR at selected angles for the yz and xz planes, respectively.

within the limitation of instrument resolution, as shown in the left inset of Fig. 1(c).

III. RESULTS AND DISCUSSION

The temperature-dependent resistivity $\rho_{xx}(T)$ of the WTe_2I single crystal measured by the standard four-probe method under selected magnetic fields with B parallel to the z axis and perpendicular to the current (along x axis) is shown in Fig. 2(a). At zero field, $\rho_{xx}(T)$ displays a metallic behavior with a moderately small residual resistivity of $\sim 73\ \mu\Omega\,\mathrm{cm}$, and the residual resistivity ratio [RRR $= \rho_{xx}(300\ \mathrm{K})/\rho_{xx}(2\ \mathrm{K})$] is about 5, which is much smaller than that of WTe_2. With the application of magnetic fields, $\rho_{xx}(T)$ is enhanced in the whole temperature range. However, different from WTe_2, WTe_2I does not exhibit a low-temperature upturn at least when the magnetic field is up to 9 T, which in WTe_2 was interpreted as an indication of a high-quality and low-charge carrier density sample [40]. Figure 2(b) presents a simulation of the zero-field resistivity with the Bloch-Grüneisen formula [41],

$$\rho(T) = \rho(0) + \rho_{\text{el-ph}}(T), \tag{1}$$

$$\rho_{\text{el-ph}}(T) = \alpha_{\text{el-ph}}\left(\frac{T}{\Theta_R}\right)^n, \tag{2}$$

where $\rho(0)$ is the residual resistivity due to defect scattering and is essentially temperature independent. $\rho_{\text{el-ph}}(T)$ is the temperature-dependent part of the resistivity, arising from an electron-phonon interaction. $\alpha_{\text{el-ph}}$ is a constant. Θ_R is a characteristic temperature usually close to the Debye temperature Θ_D. n takes an integer depending on the nature of the interaction. As shown in Fig. 2(b), neither n fixed at 2 for an electron-electron interaction and 5 for electron-phonon scattering nor an independent variable $n = 3.4$ could follow the temperature dependence in the whole measured range. Therefore, the resistivity $\rho_{xx}(T)$ behavior of WTe_2I cannot be described by simple electron-electron and electron-phonon scattering mechanisms. Moreover, with consideration of the low RRR, it seems to suggest that there are some defects in WTe_2I.

Figures 2(c) and 2(d) show the magnetic field dependence of MRs at 2 K with rotating B in both the yz plane and the xz plane, respectively. Surprisingly, we observed an unsaturated LMR. With an increase of angle θ from 0° to 90°, MR gradually decreases, reaching a maximum at $\theta = 0°$ and a minimum at $\theta = 90°$, and in the xz plane MR decreases faster towards 90° and has a maximum anisotropy of ∼1.5. Remarkably, when $\theta = 0°$, the LMR does not show any saturation with magnetic fields up to 9 T, while at $\theta = 90°$ the MR displays an obviously quadratic dependence at low fields and deviation from linear behavior at high fields. To get a clearer view of the exotic MR behavior, we plotted the B-dependent derivative of MR ($d\mathrm{MR}/dB$) curves of several typical angles in the insets of Figs. 2(c) and 2(d), respectively, and obtained B_Q and B_L determined as the intersection points of two tangent lines and a maximum in the $d\mathrm{MR}/dB$-B curves, respectively. The emergence of B_Q and B_L clearly indicates that MR at 90° is of the conventional MR behavior. These observations of the linear and conventional MR behaviors imply that the dominant scattering process is strongly anisotropic.

In order to shed more light on the anisotropic MR, we performed the temperature dependence of MR measurements on a WTe_2I single crystal. Figures 3(a)–3(c) show temperature-dependent MR with the applied magnetic fields along the x, y, and z axis, respectively. MR in all three directions gradually decreases with an increase of temperature from 2 to 300 K, and presents a quadratic dependence in high temperatures, which is the behavior of conventional MR. However, at low temperature, MR shown in Figs. 3(a) and 3(b) still possesses a quadratic one, but MR with $B \parallel z$ axis shown in Fig. 3(c) exhibits linear behavior. Moreover, we find that the linear behavior can be observed with the magnetic field down to 0.2 T at 2 K. These anisotropic MRs are different from that observed in WTe_2, in which MRs show a linear behavior with the field along the x axis and parabolic behavior with the field along the z and y axes, and the LMR were attributed to the scattering between electronlike and holelike Landau levels. Figure 3(d) shows the analysis of the resistivity curves at various temperatures with Kohler's theory [40,42],

$$\frac{\Delta\rho(T,B)}{\rho(T,0)} = F\left(\frac{B}{\rho(T,0)}\right), \tag{3}$$

where ρ is the resistivity, T is the temperature, and B is the magnetic field. According to Kohler's rule, if the carriers are from two bands featured with the same temperature dependence of the scattering rate or a single band, MR as a function of $(B/\rho_0)^2$ merges into a single curve for all temperatures. Here, we can see that the Kohler plots at all temperatures shown in Fig. 3(d) did not collapse into a single curve. This

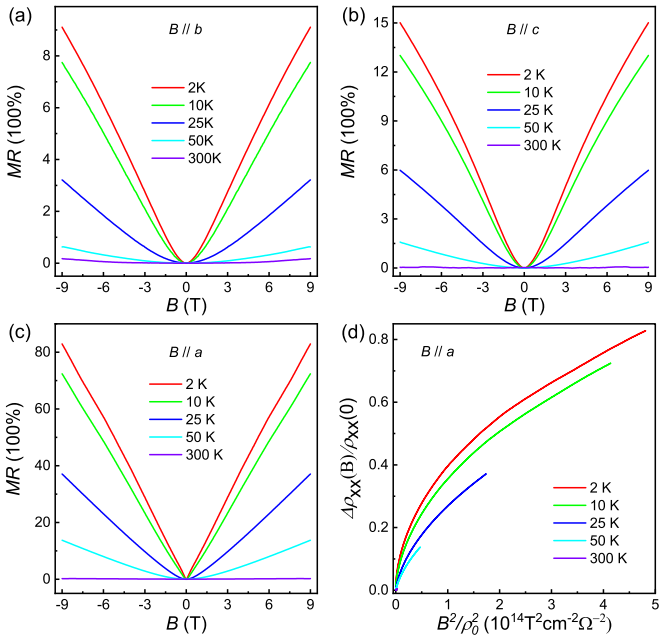

FIG. 3. (a)–(c) Magnetic field dependence of MR at various temperatures with $I \parallel x$ axis and $B \parallel x$, y, and z axis, respectively. (d) Kohler's plot of MR with $I \parallel x$ axis and $B \parallel z$ axis at all measured temperatures.

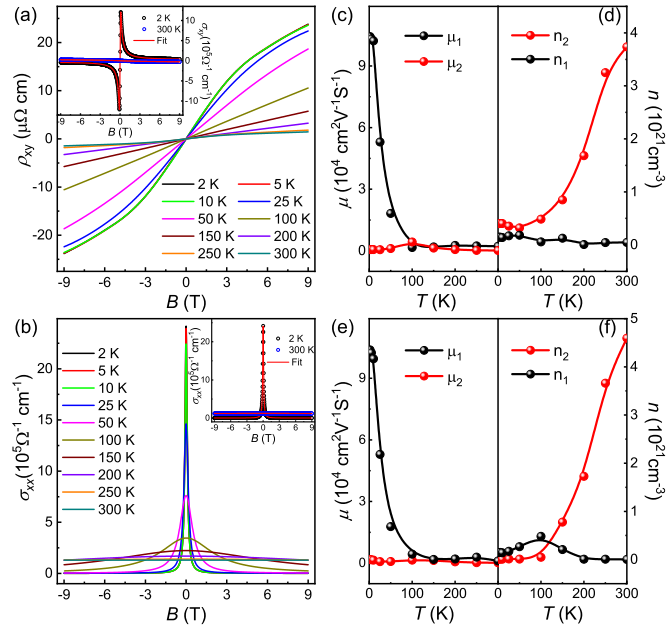

FIG. 4. (a) Magnetic field dependence of Hall resistivity ρ_{xy} at selected temperatures. The inset shows the fitting of Hall conductivity at 2 and 300 K with a semiclassical two-band model, where the black and blue dots and red lines are experimental data and fitting curves, respectively. (b) Magnetic field dependence of longitudinal conductivity σ_{xx} at selected temperatures. The inset shows the fitting of longitudinal conductivity at 2 and 300 K by conductivity fitting formula. (c)–(f) show the temperature dependence of carrier densities and mobilities extracted by fitting Hall conductivity σ_{xy} and longitudinal conductivity σ_{xx}, respectively.

confirmed that a complicated scattering mechanism participated in transport properties, which is consistent with the analysis of the zero-field resistivity by the Bloch-Grüneisen formula.

To further investigate the observed LMR in WTe_2I, we have performed a Hall-effect measurement on a single crystal of WTe_2I at various temperatures with magnetic fields along the z axis and $I \parallel x$ axis. Figures 4(a) and 4(b) show the magnetic field dependence of the Hall resistivity ρ_{xy} and the longitudinal conductivity σ_{xx} $[\sigma_{xx} = \rho_{xx}/(\rho_{xx}^2 + \rho_{xy}^2)]$ at selected temperatures from 2 to 300 K. Over the entire temperature range, ρ_{xy} has a positive slope, suggesting hole-type carriers dominate the transport process. At high temperatures, ρ_{xy} presents nearly linear behavior, while at low temperatures, ρ_{xy} has a linear behavior at low fields and nonlinear behavior at high fields. The deviation from the linear field dependence of ρ_{xy} reveals the multiband nature of WTe_2I. Thus, we analyzed the Hall conductivity σ_{xy} $[\sigma_{xy} = \rho_{xy}/(\rho_{xx}^2 + \rho_{xy}^2)]$ and longitudinal conductivity σ_{xx} using a semiclassical two-band model [43,44],

$$\sigma_{xy} = \left(\frac{n_1\mu_1^2}{1+(\mu_1 B)^2} - \frac{n_2\mu_2^2}{1+(\mu_2 B)^2}\right)eB, \tag{4}$$

$$\sigma_{xx} = \frac{en_2\mu_2}{1+(\mu_2 B)^2} + \frac{\sigma_{xx}(0) - en_2\mu_2}{1+(\mu_1 B)^2}, \tag{5}$$

where n_1 (or n_2) and μ_1 (or μ_2) denote the carrier density and mobility for two kinds of carriers, respectively. We find that both σ_{xy} and σ_{xx} can be well fitted from 2 to 300 K using the two-band model, which suggests that the semiclassical two-band model has captured the main physics. The insets of Figs. 4(a) and 4(b) show typical fitting curves of σ_{xy} and σ_{xx} at $T = 2$ and 300 K, respectively. As shown in Figs. 4(c)–4(f), the carrier densities and mobilities extracted by fitting σ_{xy} and σ_{xx} present a similar temperature-dependent tendency and the same order of magnitude. The consistency of two fitting results ensures the accuracy of the fitting results. At 2 K, $\mu_2 = 0.62 \times 10^3$ cm^2 V^{-1} s^{-1} (0.73×10^3 cm^2 V^{-1} s^{-1}) and $\mu_1 = 1.04 \times 10^5$ cm^2 V^{-1} s^{-1} (1.04×10^5 cm^2 V^{-1} s^{-1}) obtained by fitting σ_{xy} (σ_{xx}), are obviously lower than the average carrier mobility $\mu_{avg} = 1.67 \times 10^5$ cm^2 V^{-1} s^{-1} in WTe_2 [45]. The decrease of mobility probably originates from an increase of scattering due to the disorder induced by iodine intercalation.

The LMR at a high magnetic field can be generally related to two mechanisms: (i) LMR proposed by Abrikosov occurs in materials having a linear dispersion relation, only beyond the $n = 1$ Landau level [16,46], and (ii) in classical disorder models, LMR was observed in slightly disordered high-mobility or heavily disordered samples [15,47], in which the scattering of charge carriers from spatial inhomogeneities leads to mobility fluctuations and the mobility satisfies the Parrish and Littlewood (PL) criterion [15]. Recently, there was another explanation that the scattering between electronlike and holelike Landau levels also should be considered for the LMR, which is responsible for that of WTe_2 [25]. We consider here that the mobility fluctuations are the most probable cause in WTe_2I. First, according to our calculated band structure of WTe_2I in the following, we can see that there is a Dirac point near the Fermi level, but mainly the nonlinear bands cross

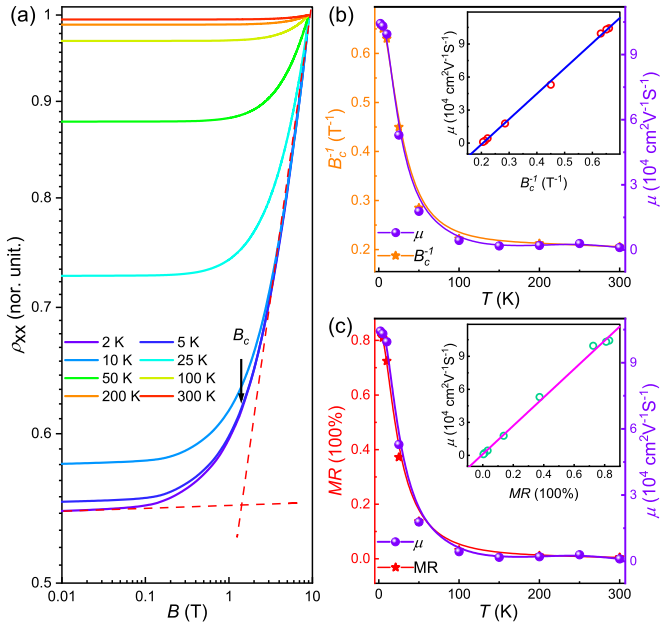

FIG. 5. (a) Log-log plot of resistance with $I \parallel x$ axis and $B \parallel z$ axis. The crossover field B_c to the linear MR is indicated by arrows. (b) Temperature-dependent B_c^{-1} and carrier mobility scaling. The inset shows the B_c^{-1} plot of carrier mobility. The blue line is a linear fit to the data. (c) Temperature dependence of MR and carrier mobility scaling. Inset: The MR plot of carrier mobility. The solid line is the linear fit to the data.

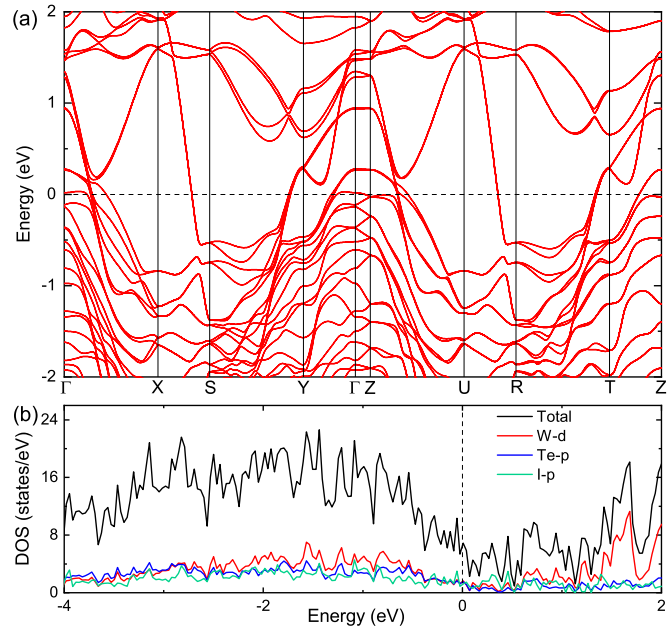

FIG. 6. The electronic structure of layered WTe_2I. (a) The band structure calculated with spin-orbit coupling along the high-symmetry directions. (b) The total and partial density of states.

the Fermi level and dominate the transport process. Second, different from WTe_2, the LMR in WTe_2I was observed under the field along the z axis other than the tungsten chains and there is no perfect electron-hole compensation. In addition, to emphasize the low-field behavior, we plotted the unconventional LMR [presented initially in Fig. 3(c)] in Fig. 5(a) on a log-log scale and obtained the crossover field B_c defined as the intersection points of two tangent lines in the ρ_{xx}-B curves and indicated by the thin arrow. Interestingly, we find that MR, mobility, and the reciprocal of crossover field B_c display a similar temperature-dependent tendency [Figs. 5(b) and 5(c)], and MR and B_c^{-1} are linearly dependent on mobility as shown in the insets of Figs. 5(b) and 5(c). These observations satisfy the conditions ($B_c \propto \langle\mu\rangle^{-1}$ and MR $\propto \langle\mu\rangle$) of the weak mobility fluctuation limit of the PL model, indicating the disorder contributes to the observed LMR, which is consistent with the above discussions. Therefore, the LMR of WTe_2I is most likely attributed to the classical origin.

Our calculated band structure of WTe_2I is in well agreement with the reported result [32]. As shown in Fig. 6(a), the calculated electronic structures with spin-orbital coupling indicate that WTe_2I is a metal. The density of states shown in Fig. 6(b) around the Fermi level is mainly contributed by W d orbitals, Te p orbitals, and I p orbitals. Different from layered WTe_2, the layered structure of WTe_2I has the nonsymmorphic space group *Pmmn* symmetry and the corresponding point group symmetry is D_{2h}. Obviously, WTe_2I cannot be a Weyl semimetal due to the space-inversion and time-reversal symmetry. On the other hand, due to the fractional translation, the commutation relation of C_{2z} $(1/2, 0, 1/2)$ and I $(1/2, 0, 1/2)$ changes from commutation to anticommutation at the high-symmetry Z point. In combination with time-reversal symmetry, any band at the high-symmetry Z point is always fourfold degenerate, which forms a Dirac point. Moreover, the Dirac point at the high-symmetry Z point is very close to the Fermi level.

IV. SUMMARY

In summary, we have grown single crystals of WTe_2I and investigated the intriguing quantum transport properties with systematic magnetotransport measurements. WTe_2I exhibits a metallic behavior with the magnetic field ranging from 0 to 9 T and significantly anisotropic MR properties. Interestingly, an exotic nonsaturating LMR was observed when $B \parallel z$ axis and $I \parallel x$ axis. The measurements of the Hall effect and first-principles calculations demonstrate that the carrier mobility conforms to the PL criterion and exclude other possible physical mechanisms. Therefore, we speculate that the observed LMR in WTe_2I is most likely attributed to the mobility fluctuations caused by the disorder. Furthermore, the band-structure calculation suggests a topological phase transition from a Weyl semimetal to Dirac metal induced by iodine intercalation.

ACKNOWLEDGMENTS

We acknowledge and thank Dong Chen for insightful comments on this manuscript. This work is supported by the Fundamental Research Funds for the Central Universities (Grant No. GK202103023), the Natural Science Foundation of Shaanxi Province (Grant No. 2022JQ-001), the Strategic Priority Research Program (B) of Chinese Academy of Sciences (Grant No.

XDB33010100), the National Natural Science Foundation of China (Grants No. 11874417, No. 11574095, No. 51901121, No. 12074213, No. 11574108 and No. 91745115), the Natural Science Foundation of Henan Province (Grant No. 182300410274), and the Major Basic Program of Natural Science Foundation of Shandong Province (Grant No. ZR2021ZD01).

W. L.Z., Y.C., and P.J.G. contributed equally to this work.

[1] H. Weng, X. Dai, and Z. Fang, J. Phys.: Condens. Matter **28**, 303001 (2016).
[2] A. Bansil, H. Lin, and T. Das, Rev. Mod. Phys. **88**, 021004 (2016).
[3] C.-K. Chiu, J. C. Y. Teo, A. P. Schnyder, and S. Ryu, Rev. Mod. Phys. **88**, 035005 (2016).
[4] W. L. Zhu, J. B. He, Y. J. Xu, S. Zhang, D. Chen, L. Shan, Y. F. Yang, Z. A. Ren, G. Li, and G. F. Chen, Phys. Rev. B **101**, 245127 (2020).
[5] X. Huang, L. Zhao, Y. Long, P. Wang, D. Chen, Z. Yang, H. Liang, M. Xue, H. Weng, Z. Fang, X. Dai, and G. Chen, Phys. Rev. X **5**, 031023 (2015).
[6] W. Zhu, X. Hou, J. Li, Y. Huang, S. Zhang, J. He, D. Chen, Y. Wang, Q. Dong, M. Zhang *et al.*, Adv. Mater. **32**, 1907970 (2020).
[7] W. Zhu, Y. Wang, J. Li, Y. Huang, Q. Dong, X. Hou, L. Zhao, S. Zhang, H. Yang, Z. Ren *et al.*, Adv. Quantum Technol. **3**, 2000020 (2020).
[8] L. Zhu, Q.-Y. Li, Y.-Y. Lv, S. Li, X.-Y. Zhu, Z.-Y. Jia, Y. Chen, J. Wen, and S.-C. Li, Nano Lett. **18**, 6585 (2018).
[9] R. Xu, A. Husmann, T. Rosenbaum, M.-L. Saboungi, J. Enderby, and P. Littlewood, Nature (London) **390**, 57 (1997).
[10] J. Hu, T. F. Rosenbaum, and J. B. Betts, Phys. Rev. Lett. **95**, 186603 (2005).
[11] M. Lee, T. F. Rosenbaum, M.-L. Saboungi, and H. S. Schnyders, Phys. Rev. Lett. **88**, 066602 (2002).
[12] J. Hu and T. Rosenbaum, Nat. Mater. **7**, 697 (2008).
[13] H. Taub, R. Schmidt, B. Maxfield, and R. Bowers, Phys. Rev. B **4**, 1134 (1971).
[14] Y.-Y. Wang, P.-J. Guo, Q.-H. Yu, S. Xu, K. Liu, and T.-L. Xia, New J. Phys. **19**, 123044 (2017).
[15] M. Parish and P. Littlewood, Nature (London) **426**, 162 (2003).
[16] A. A. Abrikosov, Phys. Rev. B **58**, 2788 (1998).
[17] T. Liang, Q. Gibson, M. N. Ali, M. Liu, R. Cava, and N. Ong, Nat. Mater. **14**, 280 (2015).
[18] J. Yang, Z.-Y. Song, L. Guo, H. Gao, Z. Dong, Q. Yu, R.-K. Zheng, T.-T. Kang, and K. Zhang, Nano Lett. **21**, 10139 (2021).
[19] M. Novak, S. Sasaki, K. Segawa, and Y. Ando, Phys. Rev. B **91**, 041203(R) (2015).
[20] L. P. He, X. C. Hong, J. K. Dong, J. Pan, Z. Zhang, J. Zhang, and S. Y. Li, Phys. Rev. Lett. **113**, 246402 (2014).
[21] J. Ping, I. Yudhistira, N. Ramakrishnan, S. Cho, S. Adam, and M. S. Fuhrer, Phys. Rev. Lett. **113**, 047206 (2014).
[22] A. Narayanan, M.D. Watson, S.F. Blake, N. Bruyant, L. Drigo, Y.L. Chen, D. Prabhakaran, B. Yan, C. Felser, T. Kong, P. C. Canfield, and A. I. Coldea, Phys. Rev. Lett. **114**, 117201 (2015).
[23] J. Feng, Y. Pang, D. Wu, Z. Wang, H. Weng, J. Li, X. Dai, Z. Fang, Y. Shi, and L. Lu, Phys. Rev. B **92**, 081306(R) (2015).
[24] M. N. Ali, J. Xiong, S. Flynn, J. Tao, Q. D. Gibson, L. M. Schoop, T. Liang, N. Haldolaarachchige, M. Hirschberger, N. P. Ong *et al.*, Nature (London) **514**, 205 (2014).
[25] Y. Zhao, H. Liu, J. Yan, W. An, J. Liu, X. Zhang, H. Wang, Y. Liu, H. Jiang, Q. Li, Y. Wang, X. Z. Li, D. Mandrus, X. C. Xie, M. Pan, and J. Wang, Phys. Rev. B **92**, 041104(R) (2015).
[26] E. Sajadi, T. Palomaki, Z. Fei, W. Zhao, P. Bement, C. Olsen, S. Luescher, X. Xu, J. A. Folk, and D. H. Cobden, Science **362**, 922 (2018).
[27] D. Kang, Y. Zhou, W. Yi, C. Yang, J. Guo, Y. Shi, S. Zhang, Z. Wang, C. Zhang, S. Jiang *et al.*, Nat. Commun. **6**, 7804 (2015).
[28] P. Wang, G. Yu, Y. Jia, M. Onyszczak, F. A. Cevallos, S. Lei, S. Klemenz, K. Watanabe, T. Taniguchi, R. J. Cava *et al.*, Nature (London) **589**, 225 (2021).
[29] Y. Wang, E. Liu, H. Liu, Y. Pan, L. Zhang, J. Zeng, Y. Fu, M. Wang, K. Xu, Z. Huang *et al.*, Nat. Commun. **7**, 13142 (2016).
[30] J. Meng, X. Chen, M. Liu, W. Jiang, Z. Zhang, J. Ling, T. Shao, C. Yao, L. He, R. Dou *et al.*, J. Phys.: Condens. Matter **32**, 355703 (2020).
[31] X.-C. Pan, Y. Pan, J. Jiang, H. Zuo, H. Liu, X. Chen, Z. Wei, S. Zhang, Z. Wang, X. Wan *et al.*, Front. Phys. **12**, 127203 (2017).
[32] P. Schmidt, P. Schneiderhan, M. Ströbele, C. P. Romao, and H.-J. Meyer, Inorg. Chem. **60**, 1411 (2021).
[33] P. E. Blöchl, Phys. Rev. B **50**, 17953 (1994).
[34] G. Kresse and D. Joubert, Phys. Rev. B **59**, 1758 (1999).
[35] G. Kresse and J. Hafner, Phys. Rev. B **47**, 558 (1993).
[36] G. Kresse and J. Furthmüller, Comput. Mater. Sci. **6**, 15 (1996).
[37] G. Kresse and J. Furthmüller, Phys. Rev. B **54**, 11169 (1996).
[38] J. P. Perdew, K. Burke, and M. Ernzerhof, Phys. Rev. Lett. **77**, 3865 (1996).
[39] J. Klimeš, D. R. Bowler, and A. Michaelides, Phys. Rev. B **83**, 195131 (2011).
[40] Y. L. Wang, L. R. Thoutam, Z. L. Xiao, J. Hu, S. Das, Z. Q. Mao, J. Wei, R. Divan, A. Luican-Mayer, G. W. Crabtree, and W. K. Kwok, Phys. Rev. B **92**, 180402(R) (2015).
[41] D. Cvijović, Theor. Math. Phys. **166**, 37 (2011).
[42] J. M. Ziman, *Electrons and Phonons: The Theory of Transport Phenomena in Solids* (Oxford University Press, Oxford, UK, 2001).
[43] N. W. Ashcroft and N. D. Mermin, *Solid State Physics* (Holt, Rinehart and Winston, New York, 1976).
[44] See Supplemental Material at http://link.aps.org/supplemental/10.1103/PhysRevB.105.125116 for fitting details.
[45] M. N. Ali, L. Schoop, J. Xiong, S. Flynn, Q. Gibson, M. Hirschberger, N. P. Ong, and R. J. Cava, Europhys. Lett. **110**, 67002 (2015).
[46] A. Abrikosov, J. Phys. A: Math. Gen. **36**, 9119 (2003).
[47] J. Hu, M. M. Parish, and T. F. Rosenbaum, Phys. Rev. B **75**, 214203 (2007).